NUCL SCI TECH (2018) 29:43
https://doi.org/10.1007/s41365-018-0370-8

Improvements to conventional X-ray tube-based cone-beam computed tomography system

Cui Zhang[1] · Xiao-Dong Pan[1] · Hong-Jie Shang[1] · Yan-Hong Luo[1] · Gong-Ping Li[1]

Received: 8 March 2017 / Revised: 29 June 2017 / Accepted: 21 July 2017 / Published online: 26 February 2018

Abstract Conventional X-ray tube-based cone-beam computed tomography (CX-CBCT) systems have great potential in industrial applications. Such systems can rapidly obtain a three-dimensional (3D) image of an object. Conventional X-ray tubes fulfill the requirements for industrial applications, because of their high tube voltage and power. Continuous improvements have been made to CX-CBCT systems, such as imaging time shortening, acquisition strategy optimization, and imaging software development, etc. In this study, a CX-CBCT system is developed. Additionally, some improvements to the CX-CBCT system are proposed based on the hardware conditions of the X-ray tube and detector. A near-detector (ND) geometry condition is employed to obtain a sharper image and larger detection area. An improved acquisition strategy is proposed to simplify operations and reduce total imaging time. In the ND geometry condition, a simplified method called FBP slice stacking (SS-FBP) is proposed, which can be applied to 3D image reconstruction. SS-FBP is time-saving relative to traditional methods. Furthermore, imaging software for the CX-CBCT system is developed in the MATLAB environment. Several imaging experiments were performed. The results suggest that the CX-CBCT system works properly, and that the above improvements are feasible and practical.

Keywords Cone-beam CT · Conventional X-ray tube · Nondestructive testing · X-ray imaging

1 Introduction

X-ray imaging has been applied in a wide range of research fields, such as medicine, biology, material science, security, and industry [1–11]. Types of X-ray imaging include radiography and computed tomography (CT). CT provides quantitative, readily interpretable data and enables the inspection of the internal structures of objects. Therefore, CT has become well established as an inspection, evaluation, and analysis tool in industry [5, 9, 12]. Based on differences in beam shapes, CT systems can be divided into three groups: parallel-beam CT (PBCT), fan-beam CT (FBCT), and cone-beam CT (CBCT). PBCT is rarely used because of its strict requirements for the collimation of the X-ray source. Recently, FBCT has been widely applied to the observation of object slices. The object should be displaced in the vertical direction for every slice to be measured. This will reduce X-ray scatter effects, but the process is time-consuming, because only one slice is measured during one object rotation. CBCT is the most common CT system in material science or industry, because it yields a hundredfold reduction in measuring time (multiple slices measured in one rotation) and produces good image quality, by using an area detector (such as FPD or CCD camera) [9, 10, 13]. In theory, CBCT scanning time is only $1/N$ the scanning time of FBCT, but

This work was supported by the Fundamental Research Funds for the Central Universities (Nos. lzujbky-2016-208 and lzujbky-2016-32).

✉ Xiao-Dong Pan
pxd@lzu.edu.cn

✉ Gong-Ping Li
ligp@lzu.edu.cn

Cui Zhang
zhangc15@lzu.edu.cn

[1] School of Nuclear Science and Technology, Lanzhou University, Lanzhou 730000, China

its X-ray utilization ratio might be N times larger than that of FBCT, while N is the number of slices.

In medicine and biology (and in some cases material science), samples measured with CT are typically made of low Z elements. Therefore, a relatively low X-ray energy is used. To improve the spatial resolution of CBCT, a micro-focus X-ray tube is often selected as the X-ray source [2, 5, 14]. However, the industrial applications of CT systems are different, and might have different requirements, such as nondestructive testing. The objects often contain metals or other high Z elements, such that a wider range of X-ray energy (corresponding to tube voltage) is required. In addition, higher X-ray tube power is demanded for measuring thick and strong absorption samples [9, 15]. As a result, micro-focus X-ray tubes have limited applicability to industrial nondestructive testing, because of their low voltage and power.

For these reasons, CX-CBCT systems have become increasingly popular in industrial nondestructive testing. The Association of Italian Maintenance (AIMAN) developed a CX-CBCT system for nondestructive testing and metrology, in collaboration with the University of Santiago de Compostela (USC). The maximum tube voltage is 225 kV, with a focal spot size of 0.4/1.0 mm. The spatial resolution of this system is 0.5 mm [16]. In addition, VARIAN has presented two cone-beam CT systems with X-ray sources of 225 kV (provided by a VARIAN HPX-450-11 X-ray tube with a focal spot size of 0.4/1.0 mm) and 950 kV (provided by a VARIAN M3 accelerator with a focal spot size of approximately 1.5 mm). These are used to study steel and aluminum parts [17]. Huang et al. [18, 19] have been committed to CBCT research. The X-ray source for the CBCT system is a Y.TU 450-D02 from YXLON with a focal spot of 2.5/5.5 mm and maximum voltage of 450 kV, while the FPD is a PaxScan-2520 from VARIAN. Although a number of CX-CBCT systems have been developed or applied, many improvements and optimizations still need to be made with respect to imaging time, acquisition strategy, image correction, and imaging software [10]. Note that the focal spot size discussed in this paper is defined by European standards.

Here, we introduce the components of the CX-CBCT system and the specific parameters for each component. Most importantly, some improvements to the CX-CBCT system are presented and discussed, through a comparison with traditional methods. Imaging results for an industrial nondestructive testing application are provided in this paper.

2 Instrument components

The CX-CBCT system consists mainly of a conventional X-ray source, a flat panel detector (FPD), a kinematic system, and other auxiliary equipment. The basic equipment and experimental setup inside the lead room are shown in Fig. 1. The details of each component will be introduced below.

2.1 X-ray source

An MXR225/22 metal ceramic X-ray tube from COMET Inc. was used in our CX-CBCT system. The maximum voltage is 225 kV, and the focal spot size is 1.0/5.5 mm, corresponding to a maximum continuous power of 640/3000 W. The target material is tungsten, a 0.8 mm beryllium window was employed to seal the vacuum. High-voltage generator is CP225 from GULMAY Ltd., while the ranges for voltage and current are 20–225 kV ($\pm$ 1%) and 0–30 mA ($\pm$ 0.5%), respectively. The emission spectra were measured before and after the X-rays passed various filters. The experimental conditions have been reported in Ref. [20], and the results are shown in Fig. 2. The produced X-ray spectrum consists of "Bremsstrahlung" and characteristic radiation, and characteristic peaks appear for the elements Cu, Ag, W, and even Pb. The characteristic peaks for Cu and Ag vanish, while the characteristic peaks for W and Pb become more prominent, because of the beam hardening caused by filters (specifically, filters with high Z elements, such as copper).

2.2 Detector

In our CX-CBCT system, an amorphous silicon flat panel detector (FPD) was used, specifically a PaxScan-1313DX from VARIAN Inc. The conversion screen was a CsI (Tl), and the detector area was 13 $\times$ 13 cm. The total pixel matrix was 1024 $\times$ 1024 (1 $\times$ 1 mode), with a pixel size of 127 $\times$ 127 μm, so that the ultimate spatial resolution was 3.94 lp/mm. Incident X-ray energy ranging from 40 to 225 keV was allowed. The maximum frame rate was 30 fps, with 16 bits of data assigned to each pixel. In addition, the total pixel matrix was 512 $\times$ 512 in 2 $\times$ 2 mode, and the maximum frame rate was up to 60 fps. Raw image acquirement and detector calibration were carried out by VARIAN-developed ViVA software, which can save or output the collected data as images or sequences.

2.3 Kinematic system

The kinematic system mainly includes a four axis motion device from BAYSIDE Co., Ltd., containing three

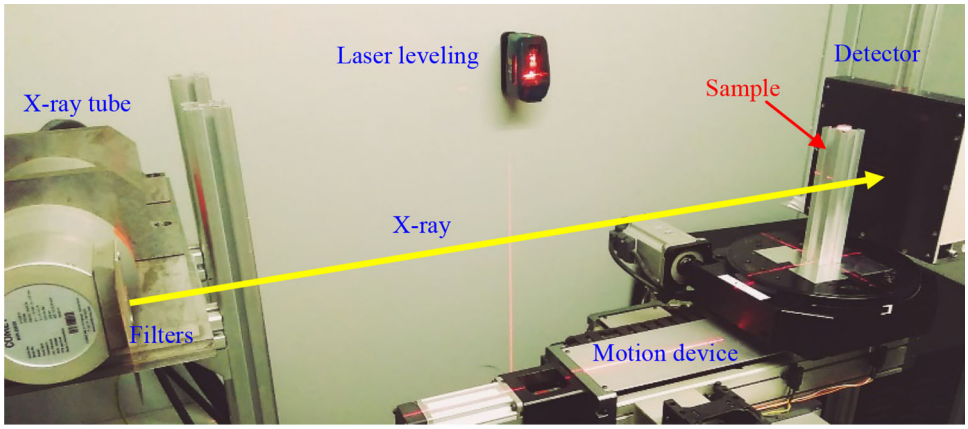

Fig. 1 (Color online) Photograph of the experimental setup

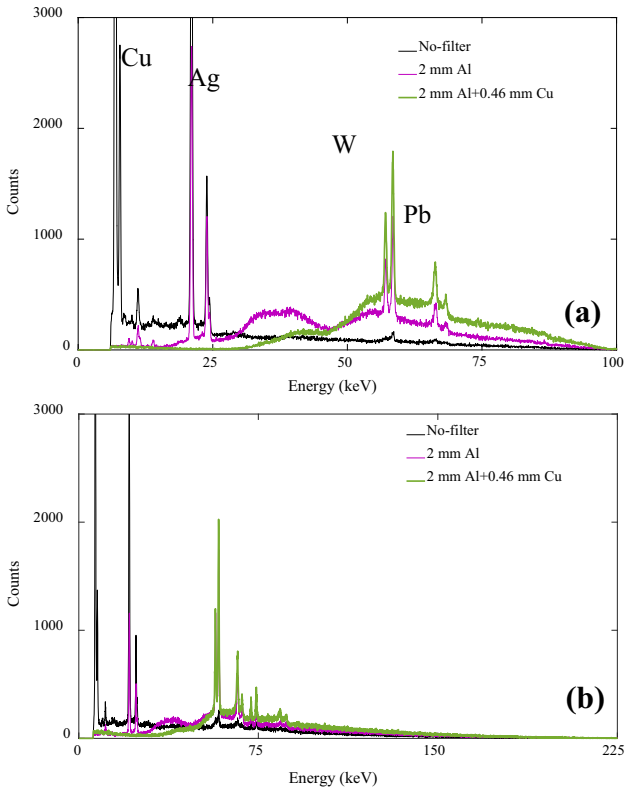

Fig. 2 (Color online) Spectra for **a** 100 kV and **b** 225 kV source before and after passing various filters (the total counts are the same when using different filters). These spectra were measured with an HPGe spectrometer, specifically a GLP-10180/07P4 from ORTEC Inc., using a full width at half maximum (FWHM) of 0.4 keV for the characteristic peak of ^{241}Am (59.6 keV) [20]

linear traveling stages and a rotational stage. The three linear traveling stages can move in the x, y and z directions with a minimal increment of 10 μm and a range of movement of 200 mm. The rotational stage can rotate about the z axis with a minimal step of 0.002°. The accuracy of the movement and rotation were guaranteed by gratings.

2.4 Others

These above components were fixed on a cast iron platform to reduce the influence of vibration. The X-ray tube and detector were fixed on sliding stages that can move back, allowing the geometry conditions to be adjusted in a larger range. The CX-CBCT platform was placed in a lead room with dimensions of 2 × 1.5 × 2 m (length × width × height). The lead shield was 10 mm thick, and the platform was laser-collimated in the horizontal and vertical directions. Inside the lead room, a camera was installed for monitoring the running state of the system. The control room had two computers: one connected to the monitoring camera and the other for controlling CT system and image reconstruction.

3 Improvements to CX-CBCT system

3.1 Geometry conditions

Geometry conditions play a vital role in the performance of a CBCT system. The X-ray tube focal spot size (d) and detector pixel size (a) significantly affect the spatial resolution of a CBCT system. By adjusting the relative positions of objects, X-ray sources, and detectors, better spatial resolution can be achieved. Two types of geometry conditions were defined according to the relative positions: the near detector (ND) geometry condition and the near source (NS) geometry condition, as shown in Fig. 3a, b, respectively. The ultimate spatial resolution of a CT system is determined primarily by parameters a, d, and geometry conditions [9, 10], which can be approximated by the following expression [21, 22]:

$$BW = \frac{\sqrt{a^2 + [d(M-1)]^2}}{M}, \quad (1)$$

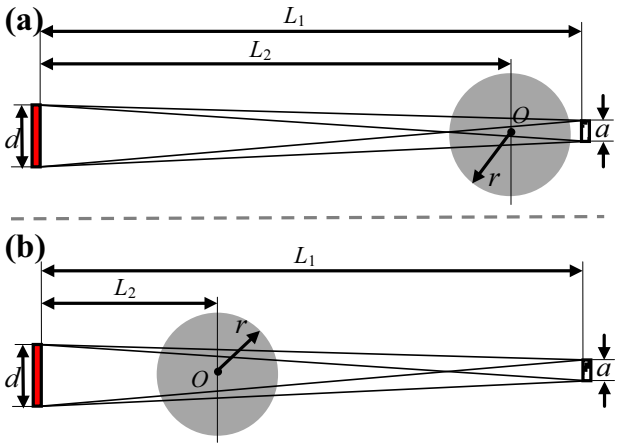

Fig. 3 Diagram of experimental geometry conditions

where BW is the effective beam width. The cut-off frequency ($1/BW$) reflects the ultimate unit resolution of lp/mm. M is magnification ($M > 1$), which equals L_1/L_2, where L_1 is the distance between the X-ray source and detector and L_2 is the distance between the X-ray source and the center of rotation. Because we used a conventional X-ray tube, whose focal spot size d (1.0/5.5 mm) is much larger than a (0.127 mm), we find that BW decreases when M is smaller. Therefore, the ultimate spatial resolution of the system is obtained when $M \to 1$. In this case, $1/BW$ tends to be 3.94 lp/mm. That is, an ND geometry condition should be used. Meanwhile, the ND geometry condition produces a larger field of view (FOV). Our previous study [23] also showed that X-ray intensity distribution is more uniform when using an ND geometry condition. However, when considering scattering effects [24] for objects composed of high Z elements, such as steel or copper, many scattered photons will be produced. When the scattered photons are recorded by the detector, spatial resolution may decline, leading to a blurred image. By increasing the distance between the object and the detector, the number of scattered photons in the detector will be effectively reduced. In this case, an NS geometry condition is more applicable.

3.2 Projection acquisition

3.2.1 Scanning strategy

For parallel-beam reconstruction, a scanning range of $\beta \in [0, \pi]$ is sufficient. However, for a fan beam, a larger scanning range is required; the minimum scanning range ($\beta_{\min}$) is [9, 25]

$$\beta_{\min} \in [-\gamma_{\max}, \pi + \gamma_{\max}], \quad (\gamma_{\max} = \arctan(r/L_2)), \qquad (2)$$

where $\gamma_{\max}$ is the maximum fan angle of the object and the center X-ray, and r is the maximum rotation radius of the object, as shown in Fig. 3. Normally, β is selected as [0, 2π], which is referred to as full-scan. This will lead to a longer scanning time and more exposure. For the ND geometry condition, $L_2 = 750$ mm and $r = 60$ mm (considered an FPD length of 13 cm); thus, $\gamma_{\max}$ is 0.08, and the minimum scanning range $\beta_{\min}$ is $[-0.08, \pi + 0.08]$, as calculated by Eq. (2). A scanning range length of $\pi + 0.16$ (called a short-scan) is sufficient for reconstruction. In addition, because $\gamma_{\max} \ll \pi$, the fan-beam condition can be approximated as a parallel-beam condition, with $\beta = [0, \pi]$ (that is, half-scan). The experimental results show that the three scanning ranges produce very similar reconstruction results for the ND geometry condition. However, short-scan and half-scan require approximately half the scanning time for the full-scan. It is very important to reduce the total imaging time for a CX-CBCT system, and reduce the exposure of the object. The reconstruction results for the three scanning ranges are shown in Fig. 4. The rotation step was chosen as 1°, an aluminum workpiece was used as the sample, and the reconstruction images were 400 × 400 pixels. $L_2 = 750$ mm and $r = 21$ mm, where $\gamma_{\max}$ was only approximately 0.03, as calculated by Eq. (2). Three quantitative parameters [26] [signal-to-noise ratio (SNR), contrast-to-noise ratio (CNR), and standard deviation (SD)] were used to perform a quantitative comparison of image quality. SNR and CNR are defined as ROI_s/SD_s and $(ROI_s - ROI_b)/SD_b$, where ROI_s and ROI_b are the mean values of the sample and the background, respectively. SD_s and SD_b are the standard deviations of the sample and the background, respectively. In addition, a coefficient of similarity (ε) [27] was employed to compare the images. Here, Fig. 4a is taken as the reference image, and ε values for Fig. 4a–c were calculated. The results are presented in Table 1. As we can see, the quality of the reconstruction images produced using the three scanning ranges are approximately the same, and the differences in the three reconstruction images are negligible. It should be noted that the approximation condition becomes inapplicable as the size of objects increases (as derived from Eq. 2). Additionally, the uniformity of the light field deteriorates to some extent as the object moves away from the center of the light field (although the uniformity of light field continues to have a maximum offset of 5% when the opening angle is $< 20°$). This can be improved by increasing the source-to-object distance.

3.2.2 Projection acquisition method

Typically, projection acquisition requires two steps [28]. The initial intensity I_0 (without a sample) and transmitted

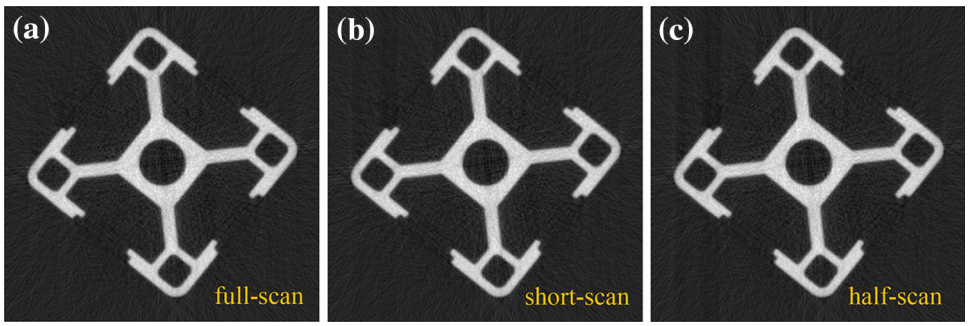

Fig. 4 Reconstruction results using the three scanning ranges

Table 1 SNR, CNR, SD_s, SD_b, and ε for the three scanning ranges

	Full-scan	Short-scan	Half-scan
SNR	2.8216	2.8093	2.7909
CNR	17.4373	17.3845	17.2618
SD_s	0.2129	0.2141	0.2157
SD_b	0.0349	0.0350	0.0353
ε	1.0000	0.9999	0.9998

intensity I (with a sample) are obtained separately, by acquiring raw images in different projection directions. The projection values (P) are calculated by the following equation:

$$P = \ln(I_0/I). \tag{3}$$

This traditional method is cumbersome and time-consuming, because of the time interval between the measurements of I_0 and I. Additionally, the running state of the X-ray tube could change during the two measurements, which could affect the value of P. Therefore, we propose a one-step projection acquisition method that can effectively decrease the effects of changes in running state. Instead of acquiring I_0 and I separately, the improved method only acquires an image for I, and selects the average intensity of the blank area as I_0 at every projection angle, thereby calculating P. This method is based on the uniformity of the light field. The mean counts for the blank area were 14,897, with a standard deviation of 129 (the coefficient of variation is 0.87%), where $L_1 = 805$ mm, $L_2 = 750$ mm, and the detector dimensions were 130 × 130 mm. Because an ND geometry condition was used, the opening angle is small, and the scattering distribution can normally be approximated as a uniform background. By analyzing the light fields with/without objects, it can be found that the scattering noise level is low and that the scattering distribution is indeed uniform. This means that if no scatter correction is conducted, the projection results obtained from the improved method are better than those for traditional methods. This is because the improved method has the same scattering background in I_0 and I, while the traditional method uses different backgrounds. A schematic diagram of the traditional and improved methods is shown in Fig. 5.

3.3 Hardening correction

As shown in Fig. 2, the beam generated by the X-ray tube is polychromatic. When the beam moves through a sample, the low energy X-rays vanish and the spectrum evolves to keep only high energy rays. This occurs because low energy photons are more rapidly attenuated than high energy photons, a phenomenon called beam hardening. A "cupping artifact" on the image will be caused by beam hardening, and therefore a proper hardening correction must be conducted. Based on the polynomial fitting method (PF) [29], an improved method called the spectrum-based polynomial fitting method (S-PF) [20] was employed to conduct hardening correction. Compared to the PF method, instead of performing a series of experiments to obtain the

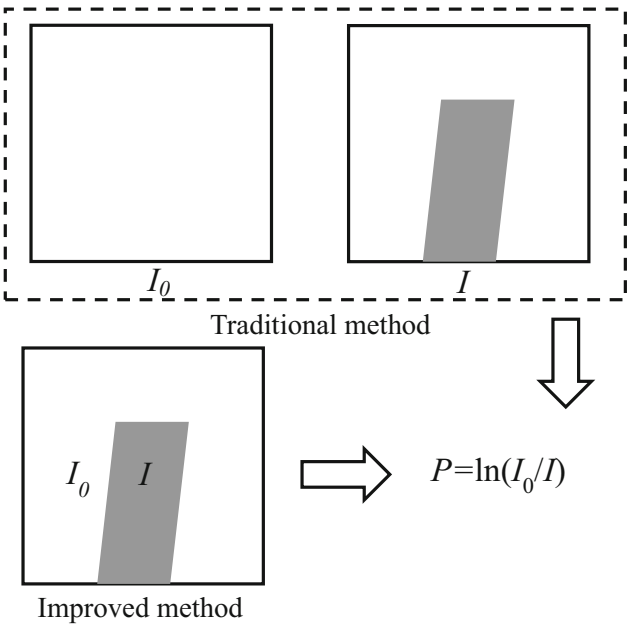

Fig. 5 Schematic diagram of traditional and improved methods for projection acquisition

relationship between polychromatic projection (P_p) and sample thickness, the S-PF method performs Monte Carlo (MC) simulations based on the measured spectrum. The S-PF method is more accurate and flexible than the PF method, because the spectrum can be measured accurately, and the components and thickness of the sample can be conveniently defined by MC software. As presented in our earlier work [20], the S-PF method can effectively eliminate cupping artifacts caused by beam hardening, especially for samples composed of a single material.

3.4 Reconstruction method

Reconstruction methods greatly affect imaging quality and time. We used a filtered back projection (FBP) algorithm [30] for our CX-CBCT system tomography image reconstruction. An FDK algorithm [31] and improved FBP slice stacking (SS-FBP) method were used for 3D reconstruction. FBP and FDK algorithms are the most commonly used methods in CT systems, because they are practical and time-saving. One of the main problems in 3D reconstruction is the complexity and quantity of data. FDK algorithms are time-saving compared with iterative algorithms [32], but a considerable amount of time (normally a few minutes) is still needed. Considering that the cone angle of X-ray beams is small in ND geometry conditions, we proposed an approximate 3D reconstruction method (SS-FBP method). We used an FBP method to reconstruct each slice of the sample. Then, a 3D image can be rapidly obtained by stacking these slices. This is made possible by eliminating the computation of small angles in the vertical direction. 3D reconstruction results from the FDK and SS-FBP methods are shown in Fig. 6a, b respectively. There is no significant difference between the two images (ε is 0.9806). The CNR values for Fig. 6a, b are 16.2746 and 15.7445, respectively. However, the reconstruction time required for FDK is 2118.30 s, while only 14.30 s is needed for SS-FBP for identical experimental conditions. The size of the 3D image is 400 × 400 × 200 pixels. These results indicate that, for approximately the same reconstruction results, the SS-FBP method using an ND geometry condition is more concise and time-saving than the FDK method.

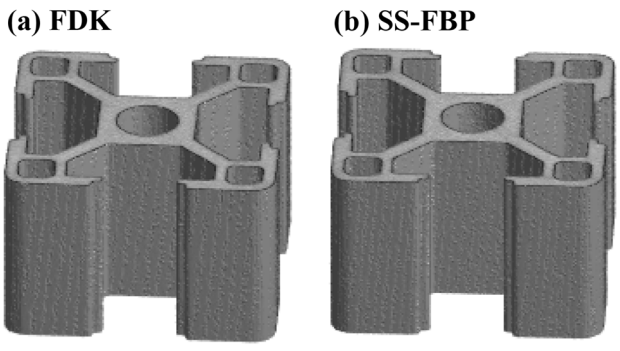

Fig. 6 3D reconstruction results for FDK and SS-FBP methods. **a** FDK. **b** SS-FBP

3.5 Software

In the MATLAB environment, data processing and imaging (DPAI) software for the CX-CBCT system was developed. The above improvements were realized in DPAI. The DPAI software includes several modules: data reading, data processing, data correction, image reconstruction, image optimization, and output. The DPAI software had a graphical user interface (GUI) that allows the program code to be conveniently optimized or modified, so that it can be adequately transplanted to other imaging techniques, such as electron imaging [33] or neutron imaging [34]. The main modules and implementation of the DPAI software are shown in Fig. 7.

The DPAI software reads the raw image sequence from FPD, acquiring the sequence at a number of projection angles. The region of interest (ROI) is selected to be reconstructed, and a raw sinogram can be obtained through the projection acquisition method introduced in Sect. 3.2. The DPAI software can obtain a single sinogram for reconstructing the tomography image by processing a single slice of data. Additionally, a set of sinograms can be obtained for 3D reconstruction by processing multiple slices of data. After noise reduction, hardening correction, and other processes for the raw sinogram, the corrected sinogram can be obtained and output for external reconstruction software, or it can be directly reconstructed as introduced in Sect. 3.4. The reconstruction results can be exhibited as tomography images (via 2D rendering) or 3D images (via volume rendering). The final reconstruction image can be obtained after some optimization processes, such as noise reduction using an adequate threshold and color gamut adjustment. These can also be saved or output in various formats.

4 Imaging results

Imaging experiments were conducted on several aluminum workpieces (as shown in Fig. 8) to demonstrate the feasibility and practicability of the above improvements, and to test the imaging capabilities of our CX-CBCT system for industrial nondestructive testing. Furthermore, 3D imaging applications with more complex samples are shown in Fig. 9. The experimental conditions are as follows: the tube voltage was 150 kV, the tube current was 0.4 mA, $d = 1$ mm, the images were 400 × 400 pixels (with a pixel size of 0.127 × 0.127 mm), a half-scan was

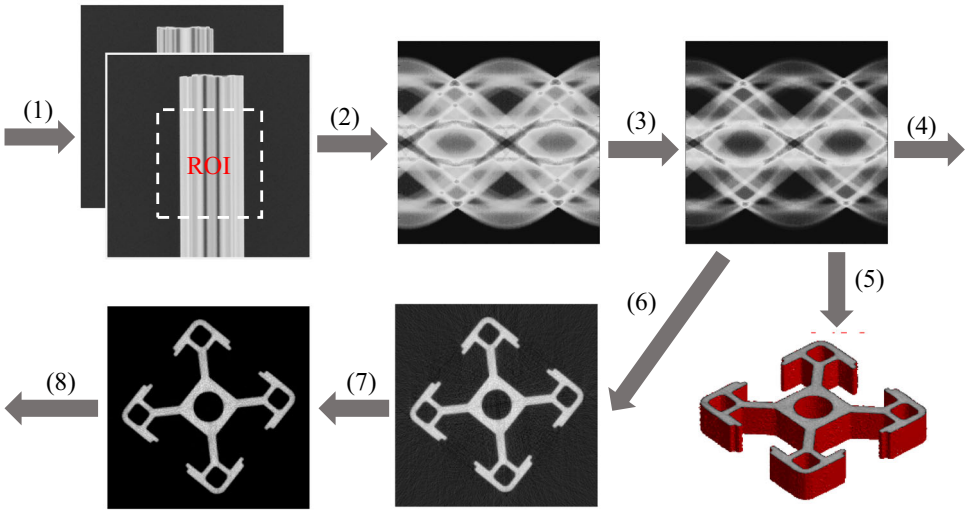

Fig. 7 (Color online) Main modules and implementation diagram of the imaging software. *1* Data reading, *2* data processing, *3* correction, *4* data output, *5* 3D reconstruction, *6* 2D reconstruction, *7* image optimization, *8* image output

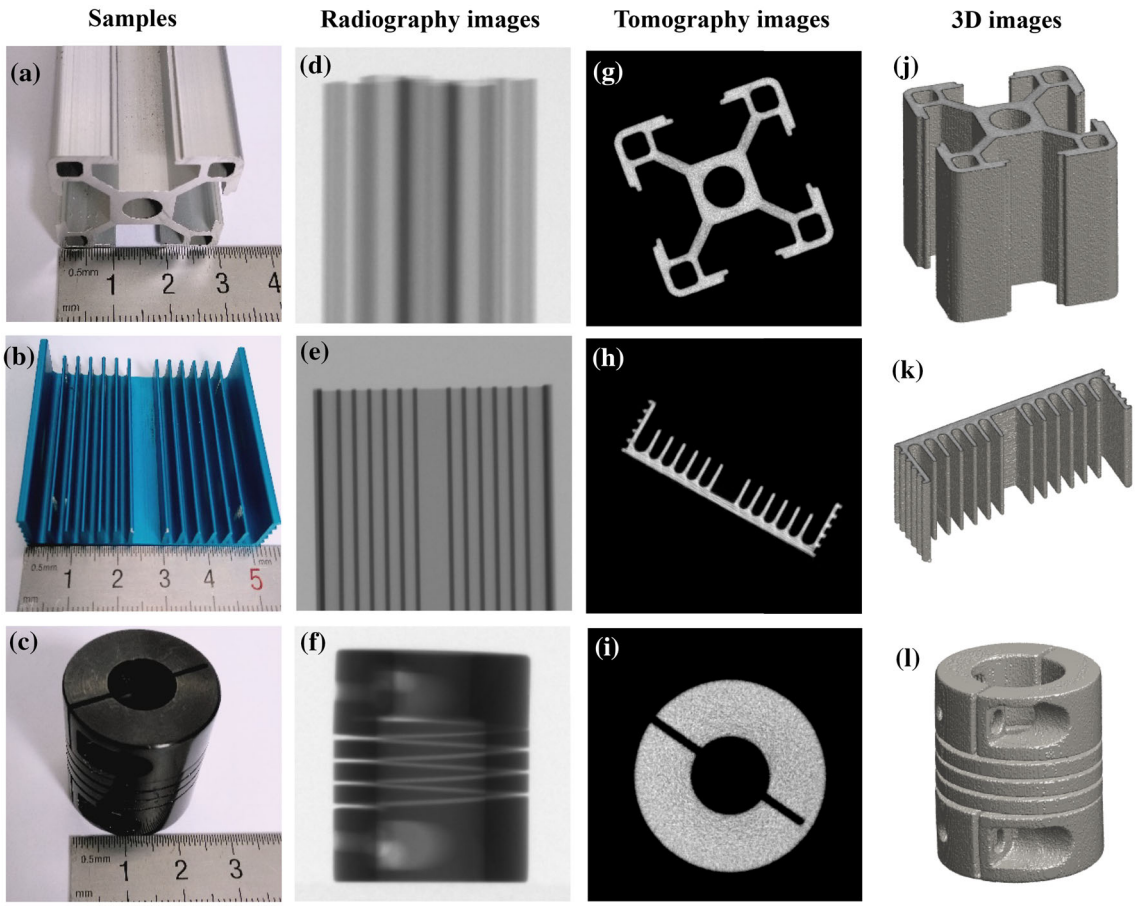

Fig. 8 (Color online) Results of imaging experiments. **a–c** Samples, **d–f** radiography images, **g–i** tomography images, **j–l** 3D images

used with a rotation step of 1° and the rotation speed of 6°/s. The detector acquisition frame rate was 6 ph/s, and the scanning time was 30 s. An ND geometry condition was adopted, where $L_2 = 750$ mm and $r < 30$ mm. The projection acquisition introduced in Sect. 3.2 was used. Tomography images and 3D images were reconstructed with the FBP and SS-FBP methods, respectively. In addition, the S-PF method was used for hardening correction.

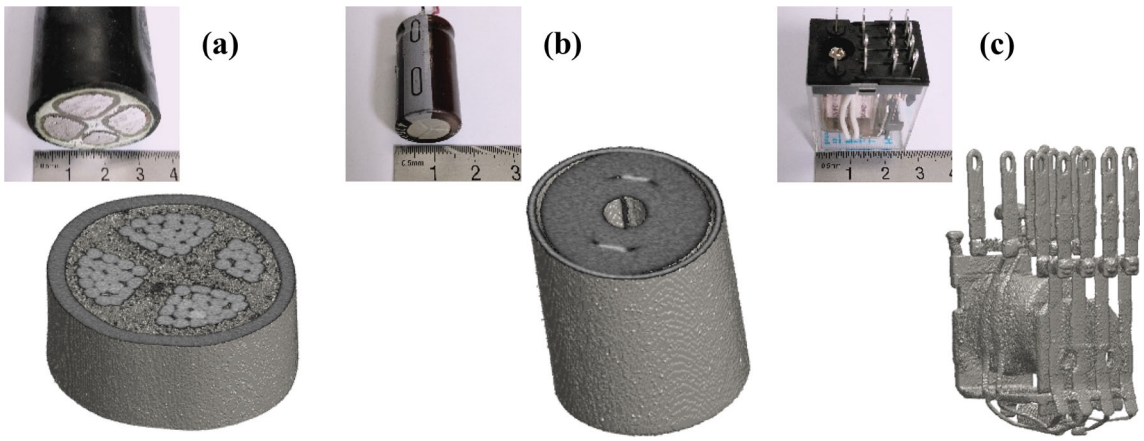

Fig. 9 3D imaging of **a** cable, **b** capacitor and **c** air-switch

Figure 8 shows a photograph, radiography image, tomography image, and 3D image for the samples, where the spatial resolution is on the order of sub-millimeters. The results verify that the CX-CBCT system works properly, and that the above improvements are feasible and practical. As shown in Fig. 9, for more complex samples (with different structures and materials), good results can still be obtained, indicating that the structure and material of the object do not affect the conclusions of this paper.

5 Discussion and conclusion

Some improvements were proposed and discussed for optimizing the CX-CBCT system. Using the ND geometry condition, spatial resolution was improved when $a \ll d$. Compared with a full-scan, a half-scan produced approximately the same reconstruction results in only half of the scanning time (in the ND geometry condition). Apart from this, the improved projection acquisition method was simplified, and scanning time was reduced compared with traditional methods. In addition, the SS-FBP method was successfully applied to 3D reconstruction for the ND geometry condition. The experimental results showed that SS-FBP could be used to correctly reconstruct the 3D image of an object, and could obtain similar results to FDK in a much shorter reconstruction time. A specific imaging software (DPAI) was developed in MATLAB. The above works could be realized in DPAI, and MATLAB is a potential development tool that can be applied to CT systems. The CX-CBCT system was successfully applied to industrial nondestructive testing, and effectively produced radiography images, tomography images, and 3D images of objects with sub-millimeter spatial resolution. Our work provides a reference for the development and improvement of CX-CBCT systems, and proposes some improvements for CX-CBCT and fast imaging. Much work must still be done to optimize the CX-CBCT system, such as scattering correction, hardening correction for multi-material and image analysis software, etc. However, there will be more industrial applications of CBCT with the development of the X-ray source and detector, specifically with the emerging of novel imaging mechanisms, such as phase-contrast imaging.

References

1. T. Flohr, C.T. Systems, Curr. Radio. Rep. **1**, 52–63 (2013). https://doi.org/10.1007/s40134-012-0005-5
2. R. Mizutani, Y. Suzuki, X-ray microtomography in biology. Micron **43**, 104–115 (2012). https://doi.org/10.1016/j.micron.2011.10.002
3. D.R. Baker, L. Mancini, M. Polacci et al., An introduction to the application of X-ray microtomography to the three-dimensional study of igneous rocks. Lithos **148**, 262–276 (2012). https://doi.org/10.1016/j.lithos.2012.06.008
4. M.K. Cho, H. Youn, S.Y. Jang et al., Cone-beam digital tomosynthesis for thin slab objects. NDT & E Int. **47**, 171–176 (2012). https://doi.org/10.1016/j.ndteint.2012.01.008
5. E. Maire, P.J. Withers, Quantitative X-ray tomography. Int. Mater. Rev. **59**, 1–43 (2013). https://doi.org/10.1179/1743280413y.0000000023
6. R. Hanke, T. Fuchs, N. Uhlmann, X-ray based methods for non-destructive testing and material characterization. Nucl. Instrum. Methods A **591**, 14–18 (2008). https://doi.org/10.1016/j.nima.2008.03.016
7. G. Kerckhofs, J. Schrooten, T. Van Cleynenbreugel et al., Validation of x-ray microfocus computed tomography as an imaging tool for porous structures. Rev. Sci. Instrum. **79**, 013711 (2008). https://doi.org/10.1063/1.2838584
8. L. Franco, J.A. Martínez-Mera, P. Tahoces et al., An own-developed CT/DR system for visualization and defect recognition in NDT, in *Proceeding of the 10th European Conference on NDT*, Moscow, 7–11 June 2010
9. J.P. Kruth, M. Bartscher, S. Carmignato et al., Computed tomography for dimensional metrology. CIRP Ann. Manuf. Technol. **60**, 821–842 (2011). https://doi.org/10.1016/j.cirp.2011.05.006

10. L. De Chiffre, S. Carmignato, J.P. Kruth et al., Industrial applications of computed tomography. CIRP Ann. Manuf. Technol. **63**, 655–677 (2014). https://doi.org/10.1016/j.cirp.2014.05.011
11. Z.Q. Chen, T. Zhao, L. Li, A curve-based material recognition method in MeV dual-energy X-ray imaging system. Nucl. Sci. Tech. **27**, 25 (2016). https://doi.org/10.1007/s41365-016-0019-4
12. D.C. Copley, J.W. Eberhard, G.A. Mohr, Computed tomography part 1: Introduction and industrial applications. NDT&E Int. **27**, 101 (1994). https://doi.org/10.1016/0963-8695(94)90319-0
13. B.C. Masschaele, V. Cnudde, M. Dierick et al., UGCT: new X-ray radiography and tomography facility. Nucl. Instrum. Methods A **580**, 266–269 (2007). https://doi.org/10.1016/j.nima.2007.05.099
14. N. Lanconelli, G. Mettivier, S.L. Meo et al., Investigation of the dose distribution for a cone beam CT system dedicated to breast imaging. Phys. Med. **29**, 379–387 (2013). https://doi.org/10.1016/j.ejmp.2012.06.001
15. A. Miceli, R. Thierry, A. Flisch et al., Monte Carlo simulations of a high-resolution X-ray CT system for industrial applications. Nucl. Instrum. Methods A **583**, 313–323 (2007). https://doi.org/10.1016/j.nima.2007.09.012
16. L. Franco, P.G. Tahoces, J.A. Martínez-Mera, Visualization software for CT: fan/cone beam and metrology applications. Proc. Eng. **63**, 779–785 (2013). https://doi.org/10.1016/j.proeng.2013.08.266
17. D. Shedlock, A. Wang, D. Nisius et al., Refinement of imaging processing of scatter correction and beam hardening tools for industrial radiography and cone beam CT, in *Digital Industrial Radiology and Computed Tomography* (Ghent University, Belgium, 22–25 June 2015)
18. K.D. Huang, H. Zhang, Y.K. Shi et al., Scatter correction method for cone-beam CT based on interlacing-slit scan. Chin. Phys. B **23**, 098106 (2014). https://doi.org/10.1088/1674-1056/23/9/098106
19. K.D. Huang, Z. Xu, D.H. Zhang et al., Robust scatter correction method for cone-beam CT using an interlacing-slit plate. Chin. Phys. C **40**, 068202 (2016). https://doi.org/10.1088/1674-1137/40/6/068202
20. C. Zhang, Y.H. Zhang, H.J. Shang et al., Measurement and application of original spectrum and transmission spectrum of X-ray tube. Atmos. Energy Sci. Technol. **50**, 1859–1865 (2016). https://doi.org/10.7538/yzk.2016.50.10.1859. **(in Chinese)**
21. M.V. Yester, G.T. Barnes, Geometrical limitations of computed tomography (CT) scanner resolution, in *Application of Optical Instrumentation in Medicine VI*, Boston, 25–27 December 1977. https://doi.org/10.1117/12.955953
22. J. Chen, Z.R. Huang, X.J. Liu et al., The relationship between the optimal magnification and the limit spatial resolution in CT system. CT Theory Appl. **23**, 37–43 (2014). https://doi.org/10.3969/j.issn.1004-4140.2014.01.005. **(in Chinese)**
23. C. Zhang, G.P. Li, X.D. Pan et al., Study on the distribution of radiation intensity of X-ray machine for industrial CT. Nucl. Tech. **38**, 090201 (2015). https://doi.org/10.11889/j.0253-3219.2015.hjs.38.090201. **(in Chinese)**
24. J.H. Siewerdsen, D.A. Jaffray, Cone-beam computed tomography with a flat-panel imager: magnitude and effects of X-ray scatter. Med. Phys. **28**, 220–231 (2001). https://doi.org/10.1118/1.1339879
25. H. Turbell, *Cone-beam Reconstruction using Filtered Backprojection*, 1st edn. (Linköping University, Sweden, 2001), pp. 13–23
26. M. Kim, J.M. Lee, J.H. Yoon et al., Adaptive iterative dose reduction algorithm in CT: effect on image quality compared with filtered back projection in body phantoms of different sizes. Korean J. Radiol. **15**, 195–204 (2014). https://doi.org/10.3348/kjr.2014.15.2.195
27. Y. Gu, Y.H. Hu, S.Q. Hao et al., Study on influence of filter back-projection on laser reflective tomography. Laser Infrared **45**, 1500–1504 (2015). https://doi.org/10.3969/j.issn.1001-5078.2015.12.018. **(in Chinese)**
28. K. Ramakrishna, K. Muralidhar, P. Munshi, Beam-hardening in simulated X-ray tomography. NDT & E Int. **39**, 449–457 (2006). https://doi.org/10.1016/j.ndteint.2006.01.006
29. G.T. Herman, Correction for beam hardening in computed tomography. Phys. Med. Biol. **24**, 81 (1979). https://doi.org/10.1088/0031-9155/24/1/008
30. B.K.P. Horn, Fan-beam reconstruction methods. Proc. IEEE **67**, 1616–1623 (1979). https://doi.org/10.1109/PROC.1979.11542
31. L.A. Feldkamp, L.C. Davis, J.W. Kress, Practical cone-beam algorithm. J. Opt. Soc. Am. A **1**, 612–619 (1984). https://doi.org/10.1364/JOSAA.1.000612
32. R. Gordon, R. Bender, G.T. Herman, Algebraic reconstruction techniques (ART) for three-dimensional electron microscopy and X-ray photography. J. Theor. Biol. **29**, 471–481 (1971). https://doi.org/10.1016/0022-5193(70)90109-8
33. C.L. Morris, N.S. King, K. Kwiatkowski et al., Charged particle radiography. Rep. Prog. Phys. **76**, 046301 (2013). https://doi.org/10.1088/0034-4885/76/4/046301
34. N. Kardjilov, I. Manke, A. Hilger et al., Neutron imaging in materials science. Mater. Today **14**, 248–256 (2011). https://doi.org/10.1016/S1369-7021(11)70139-0